Soil Moisture Active Passive (SMAP) Project

Algorithm Theoretical Basis Document

SMAP L1(B/C) Enhanced Radiometer Brightness Temperature Data Product

Julian Chaubell[1]

Contributors to this report:

Simon Yueh[1], Jinzheng Peng[2], Scott Dunbar[1], Steven Chan[1], Fan Chen[3], Jeffrey Piepmeier[2], Rajat Bindlish[2], Dara Entekhabi[4], Peggy O'Neill[2]

[1]Jet Propulsion Laboratory, California Institute of Technology, Pasadena, CA 91109 USA

[2]NASA's Goddard Space Flight Center, Greenbelt, MD 20771 USA

[3]USDA Agricultural Research Service, Beltsville, MD, USA

[4]Massachusetts Institute of Technology, Cambridge, Massachusetts, USA

Revision B

Date: May 31, 2018

Jet Propulsion Laboratory, California Institute of Technology Document# D-56287

Revision B dated May 31, 2018 contains the following updates from Revision A dated Dec 14, 2016:

1. Added section 6 describing the water/land contamination correction algorithm.

Contents

1 Introduction

The Soil Moisture Active Passive (SMAP) mission was launched on Jan 31, 2015. The mission was designed to acquire and combine L-band radar and radiometer measurements for the estimation of soil moisture with 4% volumetric accuracy (1-sigma) at a spatial resolution of better than 10 km, and the freeze-thaw state at a resolution of ~3 km (Entekhabi et al., 2010). Using the higher resolution radar measurements to disaggregate the radiometer data with a spatial resolution of 40 km results in a disaggregated brightness temperature data set with a spatial resolution 9 km, which meets the spatial resolution requirement.

On July 7, 2015 the radar stopped functioning, leaving the mission without the high spatial resolution dataset. In this document, we summarize the effort to obtain maximum value from the SMAP radiometer data given its measurement approach. This radiometer product is termed Enhanced relative to the Baseline version, in that sense.

The Baseline SMAP L1B_TB contains global surface brightness temperature estimates over a 36 km regular global grid. The aim of enhanced L1B_TB_E product is to provide an optimal interpolation of the radiometer measurements onto a global 9 km grid. The interpolation is optimal in the sense that the data are closest to what would have been measured had the instrument actually made its measurements at the interpolation points. The SMAP sampling pattern results in overlapping measurements which, together with optimal interpolation, results in more accurate estimation of brightness temperature.

Image reconstruction from discrete sampling of geophysical fields has resulted in the development of techniques that are useful for applications in microwave remote sensing as well. In Long (2003), there is an excellent statement of the problem, classification and description of the range of techniques available, including the limitations and trade-offs in microwave radiometry image reconstruction applications. In the image reconstruction problem, the surface is characterized by measurements centered at known locations but the measurement system has a broad spatial response function and a given spatial sampling pattern. Measurements also contain noise. The challenge of image reconstruction is to provide estimates of the observations at any location with a spatial response no worse than the system spatial response function and with acceptable amount of noise. An additional challenge for image reconstruction is to provide resolution enhancement. How the resolution of the reconstructed image compares to that of the measurement system depends on a number of factors but mainly it relates to the specific combination of the system response function and its spatial sampling pattern.

There are a number of algorithms directed towards the goal of image reconstruction and interpolation. A long-standing approach and one with extensive heritage in microwave radiometry is the Backus-Gilbert (BG) interpolation (Backus and Gilbert, 1970). This technique has been applied to the Special Sensor Microwave/Imager (SSM/I) measurements (Stogryn, 1978; Poe, 1990; Robison et al., 1992; Farrar and Smith, 1992; Sethmann et al., 1994; Long and Daum, 1998; Migliaccio and Gambardella, 2005) and the Tropical Rainfall Measuring Mission (TRMM) Microwave Imager (TMI) measurements (Chakraborty et al., 2008). A unique feature of the BG interpolation is that it is optimal in the sense that the resulting interpolated data is closest to what would have been measured had the

radiometer actually made the measurements with the interpolation point as its bore-sight center (Poe, 1990). In this sense and in this respect, it is superior to ad hoc or empirical interpolation techniques. Long and Brodzik (2016) studied the application of the BG algorithm for radiometer brightness image formation and reconstruction for use in the NASA-sponsored Calibrated Passive Microwave Daily Equal-Area Scalable Earth Grid 2.0 Brightness Temperature Earth System Data Record project, which generates a multisensor multidecadal time series of high-resolution radiometer products designed to support climate studies. They found that the BG provides higher spatial resolution surface brightness temperature images with smaller total error compared with conventional drop-in-the-bucket gridded image formation.

When the data are uniformly sampled in space, the resolution of the reconstructed image is limited by the well-known Nyquist uniform sampling theorem. However, when the spatial sampling is non-uniform and there is oversampling in space, "resolution enhancement algorithms provide improved resolution images by taking advantage of oversampling and the response characteristics of the aperture function to reconstruct the underlying surface function sampled by the sensor" (Long, 2003). Specifically, if the density of measurements is higher than the resolution of the instrument, then it may be possible to reconstruct an image by weighted combination of surrounding measurements that has a higher spatial resolution than the original data (Robinson et al., 1992). The resolution enhancement capabilities of reconstruction or interpolation algorithms depend on the sampling pattern and the overlap in the response functions of the instrument at measurement locations. In general, the higher the sampling density (leading to more overlap in the measurements), the better the possibility of resolution enhancement, according to Long and Daum (1998).

The SMAP radiometer's conical scan and the Low-Earth orbit result in a spatial sampling that is irregular. The distributional characteristics of the spatial sampling are different along- and across-track. The SMAP radiometer does provide oversampling of the imaged surface in some situations, but is under sampled in others. The nominal antenna footprint is 39 km by 47 km based on half-power contribution, while the spacing between cross track samples is typically 11 km, the spacing along track varies from as little as 20 km to as much as 28 km. Long (2001) provides a detailed and extensive summary of specific features of random fields with non-uniform sampling. In that paper he expands on Irregular Sampling Theory and provides the relationship between the properties of the irregular sampling of a random field with an operator and the recoverable frequency.

In this ATBD we present an implementation of the BG optimal interpolation algorithm for interpolating the SMAP radiometer measurements onto a Fixed-Earth EASEv2 grid. Since image reconstruction includes a trade-off between noise and resolution, we also report on the estimated noise variances in the interpolated fields based on the noisy measurements.

In the following section we summarize the polarimetry formulation of the BG interpolation. This formulation, by Dr. Simon Yueh, follows the formulation in Poe's paper for single polarization [3] and extends it to apply for the full Stokes vector.

2 Optimal Interpolation of Polarimetric Brightness Temperatures

The measurements of polarimetric brightness temperature, characterized by the Stokes vector, are related to Mueller matrix ($\overline{\overline{G}}$) of the antenna pattern by

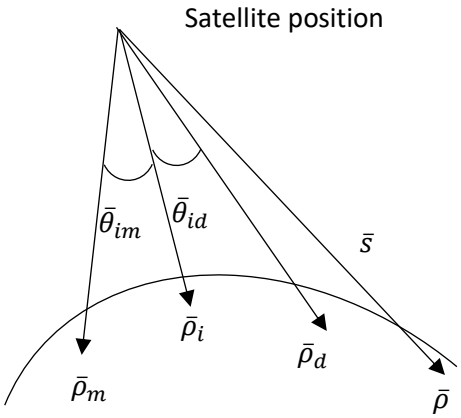

Figure 1: Satellite geometry. $\bar{\rho}$ represents a point on Earth, the domain of integration. $\bar{\rho}_d$ represents the interpolating location, a point on the EASE2 grid. $\bar{\rho}_i$ and $\bar{\rho}_m$ represent two SMAP footprints.

$$\begin{bmatrix} T_{AV} \\ T_{AH} \\ U_A \\ V_A \end{bmatrix} = \int \overline{\overline{G}} \begin{bmatrix} T_{BV} \\ T_{BH} \\ U \\ V \end{bmatrix} dA \qquad (2.1)$$

The integration is carried out over the surface. Note that in all the integrals, for simplicity, we are not including the projection factor $\bar{s}.\boldsymbol{\rho}\ /|\bar{s}|$ where $\boldsymbol{\rho}$ is the unit vector position corresponding to $\bar{\rho}$ and $\bar{s}$ is the vector pointing from the satellite to $\bar{\rho}$, see Figure 1.

The modified Mueller Matrix of the antenna pattern is

$$\overline{\overline{G}} = \begin{bmatrix} |G_{VV}|^2 & |G_{VH}|^2 & \mathrm{Re}(G_{VH}G_{VV}^*) & \mathrm{Im}(G_{VH}G_{VV}^*) \\ |G_{HV}|^2 & |G_{HH}|^2 & \mathrm{Re}(G_{HH}G_{HV}^*) & \mathrm{Im}(G_{HH}G_{HV}^*) \\ 2\,\mathrm{Re}(G_{VV}G_{HV}^*) & 2\,\mathrm{Re}(G_{VH}G_{HH}^*) & \mathrm{Re}(G_{VV}G_{HH}^* + G_{VH}G_{HV}^*) & -\mathrm{Im}(G_{VV}G_{HH}^* - G_{VH}G_{HV}^*) \\ 2\,\mathrm{Im}(G_{VV}G_{HV}^*) & 2\,\mathrm{Im}(G_{VH}G_{HH}^*) & \mathrm{Im}(G_{VV}G_{HH}^* + G_{VH}G_{HV}^*) & \mathrm{Re}(G_{VV}G_{HH}^* - G_{VH}G_{HV}^*) \end{bmatrix} \qquad (2.2)$$

For the BG interpolation algorithm, we will approximate the Mueller Matrix at the interpolation location,$\bar{\rho}_d$, by

$$\bar{\bar{G}}_d = \bar{\bar{G}}(\bar{\rho}_d, \bar{\rho}) = \sum_{i=1}^{N} a_i \bar{\bar{G}}_i = \sum_{i=1}^{N} a_i \bar{\bar{G}}(\bar{\rho}_i, \bar{\rho}) \tag{2.3}$$

where $\bar{\rho}_i$with $i = 1 \ldots . . N$ are the SMAP measurement locations and $\bar{\rho}$ is a point in the integration domain. In equation (2.3) and in the following, we use $\bar{\bar{G}}_i$to refer to $\bar{\bar{G}}(\bar{\rho}_i, \bar{\rho})$, the antenna pattern centered at $\bar{\rho}_i$ and evaluated at $\bar{\rho}$.

The Stokes vector of the antenna temperature at the interpolated location is

$$\begin{aligned} \begin{bmatrix} T_{AV} \\ T_{AH} \\ U_A \\ V_A \end{bmatrix} &= \int \overline{\overline{G}}_d \begin{bmatrix} T_{BV} \\ T_{BH} \\ U \\ V \end{bmatrix} dA \\ &= \int \sum_{i=1}^{N} a_i \overline{\overline{G}}_i \begin{bmatrix} T_{BV} \\ T_{BH} \\ U \\ V \end{bmatrix} dA \end{aligned} \tag{2.4}$$

The error of the interpolated Stokes vector is

$$\mathrm{D}T_A = \int (\overline{\overline{G}}_d - \sum_{i=1}^{N} a_i \overline{\overline{G}}_i) \begin{bmatrix} T_{BV} \\ T_{BH} \\ U \\ V \end{bmatrix} dA \tag{2.5}$$

2.1 Constraint on Energy Conservation for Each Polarization

For a lossless antenna, energy conservation requires:

$$\int |G_{VV}|^2 + |G_{HV}|^2 dA = 1 \tag{2.6}$$
$$\int |G_{VH}|^2 + |G_{HH}|^2 dA = 1 \tag{2.7}$$

Therefore, we can impose the following conditions for the Mueller Matrix of the antenna pattern at the interpolation location:

$$\int G_{d11} + G_{d21}\, dA = \int dA \sum_{i=1}^{N} a_i (G_{i11} + G_{i21}) = 1$$
$$\int G_{d12} + G_{d22}\, dA = \int dA \sum_{i=1}^{N} a_i (G_{i12} + G_{i22}) = 1 \quad (2.8)$$

We can estimate the expansion coefficients, a_i, by minimizing the following cost function

$$e = \int dA \sum_{j,k=1}^{4} \left(G_{djk} - \sum_{i=1}^{N} a_i G_{ijk} \right)^2 + \lambda_1 \left[\int dA \sum_{i=1}^{N} a_i (G_{i11} + G_{i21}) - 1 \right] + \lambda_2 \left[\int dA \sum_{i=1}^{N} a_i (G_{i12} + G_{i22}) - 1 \right] \quad (2.9)$$

where G_{djk} are the elements of the Muller matrix centered at $\bar{\rho}_d$ and G_{ijk} are the elements of the Muller matrix centered at $\bar{\rho}_i$.

The Lagrange multipliers, λ_1 and λ_2, are used to introduce the constraint defined by Eq. (2.8).

Taking the partial derivative leads to the following equation:

$$\frac{\partial \varepsilon}{\partial a_i} = 2 \sum_{m=1}^{N} g_{im} a_m - 2 v_i + \lambda_1 u_{i1} + \lambda_2 u_{i2} \quad (2.10)$$

Where

$$g_{im} = \sum_{j,k=1}^{4} \int dA G_{jk}(\bar{\rho}_i, \bar{\rho}) G_{jk}(\bar{\rho}_m, \bar{\rho})$$
$$v_i = \sum_{j,k=1}^{4} \int dA G_{jk}(\bar{\rho}_i, \bar{\rho}) G_{jk}(\bar{\rho}_d, \bar{\rho}) \quad (2.11)$$
$$u_{i1} = \int dA G_{11}(\bar{\rho}_i, \bar{\rho}) + G_{21}(\bar{\rho}_i, \bar{\rho})$$
$$u_{i2} = \int dA G_{12}(\bar{\rho}_i, \bar{\rho}) + G_{22}(\bar{\rho}_i, \bar{\rho})$$

Setting the partial derivative equal to zero, we obtain

$$\bar{\bar{g}} \times \bar{a} = \bar{v} - \lambda_1 \bar{u}_1 - \lambda_2 \bar{u}_2 , \quad (2.12)$$

where $\bar{\bar{g}}$ is the matrix with elements $g_{im}, i = 1 \ldots N$ and $m = 1 \ldots N$, $\bar{a}$ is the vector of coefficients $a_i, i = 1 \ldots N$ and $\bar{v}, \bar{u}_1, \bar{u}_2$ are vectors with elements v_i, u_{i1} and $u_{i2}, i = 1 \ldots N$ respectively.

In other words,

$$\bar{a} = \bar{\bar{g}}^{-1} \times \bar{v} - \lambda_1 \bar{\bar{g}}^{-1} \times \bar{u}_1 - \lambda_2 \bar{\bar{g}}^{-1} \times \bar{u}_2 \tag{2.13}$$

Applying the constraints described in Eq. (2.8)

$$\begin{aligned} \bar{u}_1^T \times \bar{a} = 1 = \bar{u}_1^T \times \bar{\bar{g}}^{-1} \times \bar{v} - \lambda_1 \bar{u}_1^T \times \bar{\bar{g}}^{-1} \times \bar{u}_1 - \lambda_2 \bar{u}_1^T \times \bar{\bar{g}}^{-1} \times \bar{u}_2 \\ \bar{u}_2^T \times \bar{a} = 1 = \bar{u}_2^T \times \bar{\bar{g}}^{-1} \times \bar{v} - \lambda_1 \bar{u}_2^T \times \bar{\bar{g}}^{-1} \times \bar{u}_1 - \lambda_2 \bar{u}_2^T \times \bar{\bar{g}}^{-1} \times \bar{u}_2 \end{aligned} \tag{2.14}$$

We have two linear equations for the two Lagrange multipliers.

$$\begin{aligned} \lambda_1 \bar{u}_1^T \times \bar{\bar{g}}^{-1} \times \bar{u}_1 + \lambda_2 \bar{u}_1^T \times \bar{\bar{g}}^{-1} \times \bar{u}_2 = \bar{u}_1^T \times \bar{\bar{g}}^{-1} \times \bar{v} - 1 \\ \lambda_1 \bar{u}_2^T \times \bar{\bar{g}}^{-1} \times \bar{u}_1 + \lambda_2 \bar{u}_2^T \times \bar{\bar{g}}^{-1} \times \bar{u}_2 = \bar{u}_2^T \times \bar{\bar{g}}^{-1} \times \bar{v} - 1 \end{aligned} \tag{2.15}$$

The values of λ_1 and λ_2 can be substituted into Eq. (2.13) to obtain the expansion coefficients, a_i.

We have to take care of a special case. That is when the antenna patterns for vertical and horizontal polarizations are the same, i.e., $\bar{u}_1 = \bar{u}_2$. Then the determinant of the two equations will be zero and it will be problematic to solve these two equations, Eq. (2.15). However, in this special case we can let $\lambda_1 = \lambda_2 = \lambda$ to obtain the value of λ as

$$\lambda = \frac{\bar{u}^T \times \bar{\bar{g}}^{-1} \times \bar{v} - 1}{2\bar{u}^T \times \bar{\bar{g}}^{-1} \times \bar{u}} \tag{2.16}$$

Then the vector of the expansion coefficients becomes

$$\bar{a} = \bar{\bar{g}}^{-1} \times \bar{v} + \left(\frac{1 - \bar{u}^T \times \bar{\bar{g}}^{-1} \times \bar{v}}{\bar{u}^T \times \bar{\bar{g}}^{-1} \times \bar{u}}\right) \bar{\bar{g}}^{-1} \times \bar{u} \tag{2.17}$$

This expression is the same as Eq. (14) in (Poe, 1990).

2.2 Constraint on Total Power

Rather than applying the energy conservation condition for each polarization (Eq. 2.8), we can choose to apply the constraint on total power only:

$$\int |G_{VV}|^2 + |G_{HV}|^2 + |G_{VH}|^2 + |G_{HH}|^2 \tag{2.18}$$

In other words,

$$\int G_{d11} + G_{d21} + G_{d12} + G_{d22} dA \tag{2.19}$$

Following the same approach to solve the expansion coefficients using the Lagrange multiplier method for the case $\lambda_1 = \lambda_2 = \lambda$, we obtain

$$\bar{\bar{a}} = \bar{\bar{g}}^{-1} \times \bar{v} + \left(\frac{2 - \bar{u}^T \times \bar{\bar{g}}^{-1} \times \bar{v}}{\bar{u}^T \times \bar{\bar{g}}^{-1} \times \bar{u}}\right) \bar{\bar{g}}^{-1} \times \bar{u} \quad , \tag{2.20}$$

where

$$u_i = \int dA G_{11}(\bar{\rho}_i, \bar{\rho}) + G_{21}(\bar{\rho}_i, \bar{\rho}) + G_{12}(\bar{\rho}_i, \bar{\rho}) + G_{22}(\bar{\rho}_i, \bar{\rho}) \tag{2.21}$$

with $i = 1 \ldots N$.

3 Implementation

The L1B_TB_E product provides, among other important quantities, the interpolated brightness temperature on a 9km EASE2 grid. L1B_TB_E processor applies the BG optimal interpolation to obtain the brightness temperature at the grid points. Equations (2.11) and (2.21) are the bases for the direct evaluation of the vector *u* and *v* and the matrix $\bar{\bar{g}}$, necessary to obtain the coefficients *a*. These calculations can be computationally very expensive. In order to make our algorithm more computationally efficient, we implemented the following approximations:

1) The computation of the components of the vector *u* involves only the integration of the beam pattern centered at the selected SMAP measurements location $\bar{\rho}_i$ and it can be considered constant for all locations.

$$u_i = \int dA G_{11}(\bar{\rho}_i, \bar{\rho}) + G_{21}(\bar{\rho}_i, \bar{\rho}) + G_{12}(\bar{\rho}_i, \bar{\rho}) + G_{22}(\bar{\rho}_i, \bar{\rho}) \sim \tilde{u}, \text{for all } i = 1 \ldots N.$$

We approximate the vector *u* with the vector $\hat{u}$, $u \sim \hat{u}$, where $\hat{u}$ has all the components equal to $\tilde{u}$. In our algorithm we use $\tilde{u}$ = 1.836 to be consistent with the current version antenna pattern used for antenna pattern (or side lobe) correction matrix. The value is obtained by integrating the antenna pattern over the earth surface only.

2) The components of the vector *v* involve the integration of the product of the beam pattern centered at the measurements $\bar{\rho}_i$ and the beam pattern centered at the target point $\bar{\rho}_d$. In our algorithm, we expressed the components of the vector *v* as a function of the angular separation θ_{id}, see Figure 1, to reduce the integration to the evaluation of an analytic expression. This analytic expression was obtained by precomputing equation

(2.11) for a fixed $\bar{\rho}_i$ for a great set of $\bar{\rho}_d$,Figure 2. A one-dimensional Gaussian function, with angular separation dependence, was then fit to obtain the final analytic expression.

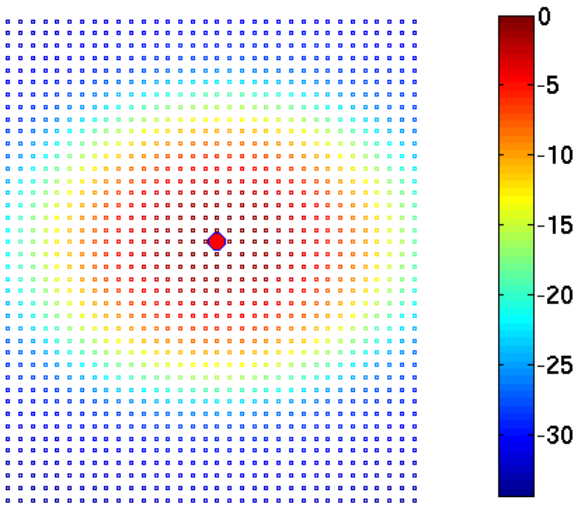

Figure 2: Value of v, in dB's, computed for a fixed SMAP measurement location $\bar{\rho}_i$ (center point) and for a set of neighbors points. The separation between points is 3km.

$$v_i = \sum_{j,k}^{4} \int dA G_{jk}(\bar{\rho}_i, \bar{\rho}) G_{jk}(\bar{\rho}_d, \bar{\rho}) \sim \tilde{v}(\theta_{id}) = \hat{v}_i$$

where

$$\tilde{v}(\theta_{id}) = ae^{-(\theta_{id}/c)^2},$$

and *a* and *c* are pre-computed coefficients, $\hat{v}$ is the vector with components $\hat{v}_i$. In our algorithm we use *a* = 867.2 and *c* = 1.951.

3) The computation of the elements of the matrix $\bar{\bar{g}}$ involves the integration of the product of the beam pattern centered at the measurements $\bar{\rho}_i$ and the beam pattern centered at $\bar{\rho}_m$. As before, we expressed the elements of the matrix G as a function of the angular separation ϑ_{im}, Figure 1, to reduce the integration to the evaluation of an analytic expression.

$$g_{im} = \sum_{j,k}^{4} \int dA G_{jk}(\bar{\rho}_i, \bar{\rho}) G_{jk}(\bar{\rho}_m, \bar{\rho}) \sim \tilde{v}(\theta_{im}) = \hat{g}_{im}$$

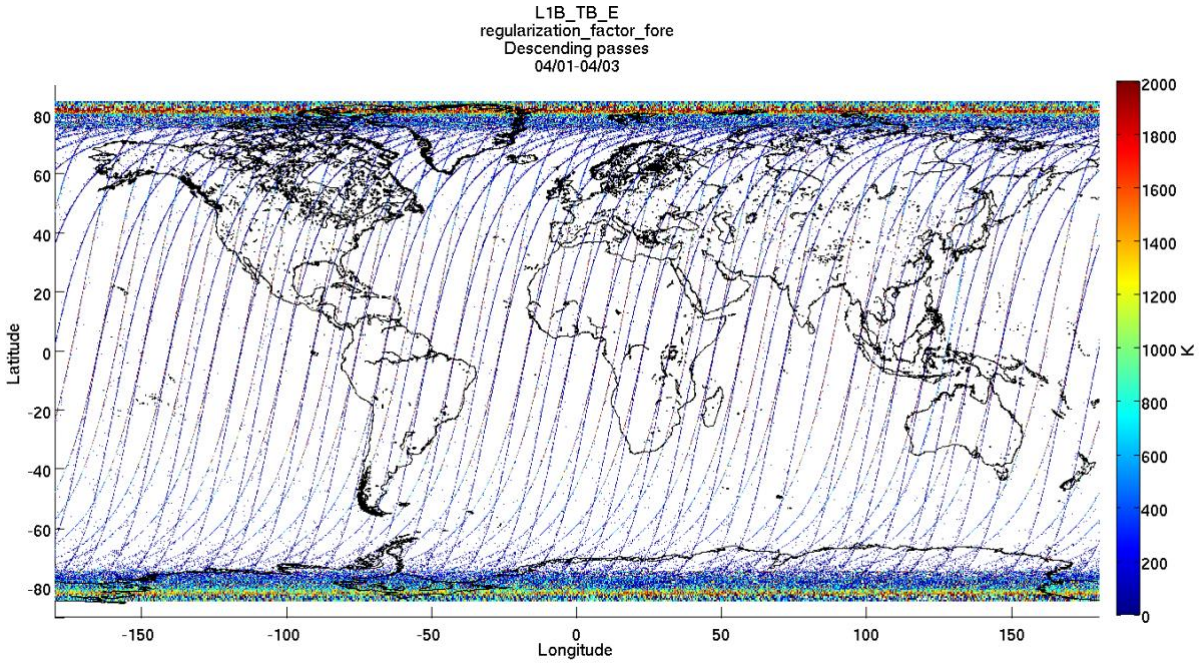

Figure 3:Map of the regularization factor for forward look on descending passes. The map shows the location where regularization was applied.

where $\tilde{v}$ is defined as before and $\hat{g}$ is the matrix with elements $\hat{g}_{im}$.

It is important to note that our beam patterns do not satisfy the total power conservation equation (2.19) exactly and therefore the corresponding normalization correction in equation (2.20) needs to be done. In other words,

$$\int \mathrm{dA}(|G_{VV}|^2 + |G_{VH}|^2 + |G_{HV}|^2 + |G_{HH}|^2) = E = 1.836$$

.

Note that the expression of the vector coefficient *a* requires the inversion of the matrix $\bar{\bar{g}}$., which for some distributions of the points $\bar{\rho}_i$ shows to have a poor condition number. In those cases, we replace the matrix $\bar{\bar{g}}$ with the generalized matrix

$$G^g = (\bar{\bar{g}}^T \bar{\bar{g}} + \omega\, I)^{-1} \bar{\bar{g}}^T,$$

where ω is a regularization parameter and *I* is the identity matrix. The magnitude of ω is set to the minimum that results in stable $\hat{a}$ and minimum beam broadening effect in the interpolated field. Note that for ω = 0, $G^g = \bar{\bar{g}}^{-1}$. For the SMAP geometry, regularization is applied mostly at the boundaries of the swath when the scan angles are close to 90^o or 270^o, see Figure 3.

With all the above the approximated vector $\hat{a}$ is given by

$$\hat{a} = G^g.\hat{v} + \left(\frac{E - \hat{u}^T G^g \hat{v}}{\hat{u}^T G^g \hat{u}}\right) G^g.\hat{u}.$$

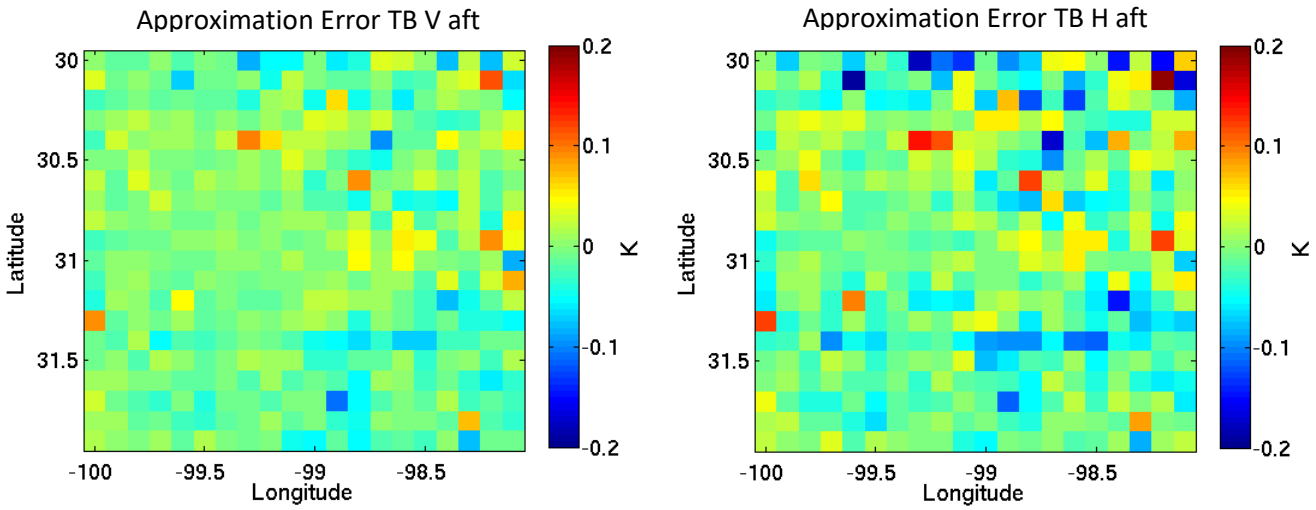

Figure 4: Approximation errors. Left: For TB V pol. Right: For TB H pol.

In order to validate our approximations, we interpolated the brightness temperatures over a small set of points (20x20 points), first, using the coefficients $\bar{a}$ and then, using the approximated coefficients $\hat{a}$. We then computed the differences which are displayed in Figure 4. Table 1 shows the approximation error statistics for TB V and H polarizations. It is important to note that the processing of 400 points using $\bar{a}$ took ~52 hours, while the processing of the same amount of points using $\hat{a}$ took 35 seconds.

	TB H	TB V
Mean	-0.012	-0.006
STD	0.046	0.029
RMS	0.047	0.029

Table 1: Approximation error statistics for TB H and V polarization.

3.1 Points Selection

The accuracy of the algorithm depends on the number of points used to perform the BG interpolation. There is a tradeoff in the accuracy of the signal reconstruction, the computational requirements, and the area included in the reconstruction of the interpolated values. This was explicitly explored in Long and Daum (1998). Considering that our function $\tilde{v}(\theta_{id})$ decreases about 10 dB for angles greater than 3 degrees we decided to restrict our algorithm to points that are within one SMAP revolution apart. We analyzed using three points on the same revolution, for example the three closest blue points in Figure 5. We found this arrangement produced biased results because the interpolating point was observing information from only one side instead of observing information from all the surrounding area. In particular, this effect was observed in coastal regions when the target point was on land and the chosen SMAP measurements were located over the ocean. Regarding the computational time, doubling the number of SMAP measurements to reconstruct the signal, doubles the running time.

Currently, with a six-point arrangement, see Figure 5, it takes ~5 hours to process a half-orbit. After all those considerations it was decided to work with a six point arrangement, see Figure 5.

To quickly search for the closest SMAP measurement to a given grid point in the discrete computation grid (referred as the target point), the entire latitude/longitude grid was divided into 0.3x0.3 degree cells, 600x1200 cells covering the entire globe. Then the SMAP data located in each cell was indexed. Thus, for a target point located into a specific 0.3x0.3-degree cell, the search was limited to only the indexed set of SMAP measurements contributing to that cell and its neighbor cells, see Figure 6. Since the spacing between cross track samples is typically 11 km, the spacing along track varies from as little as 20 km to as much as 28 km, then we can guarantee to find at least one SMAP measurement within the searching area.

The selection of the six points goes as follows:

1) We locate the cell that contains the target point (red point in Figure 5). We identify this cell as cell *(i,j)* in Figure 6. Then we look for the closest point to the target point in the cell that contains it and as well as its neighbor cells.
2) Once the closest point is obtained, Figure 5, the closest two neighbors on the same SMAP revolution are selected. In other words, if the closest point lies on revolution *r* and corresponds to scan angle *s* then we select the neighbors *(r, s+1)* and *(r, s-1)*. If *(r, s+1)* is a fill value (-9999.0) then we select *(r, s+2)*. Again, if *(r, s-1)* is a fill value then we select *(r, s-2)*.
3) With steps 1) and 2) we complete the selection of three points.
4) We then perform a new search for the closest point that does not lie on revolution *r.* Once this point is found, we complete the new set of three points as in 2).
5) If after the selection of the six points we still have a fill values, then the Tb at the target points is set to a fill value.

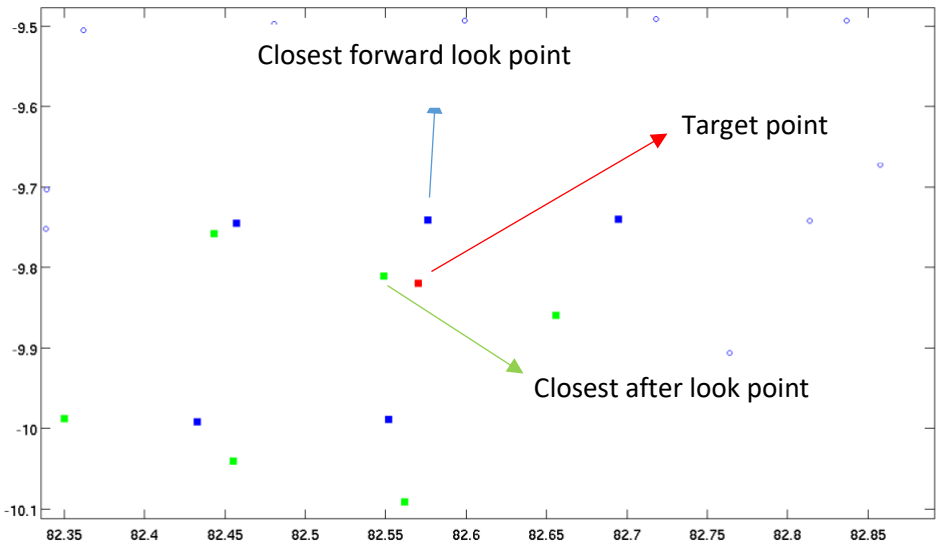

Figure 5: Selected points diagram.

Note that point selection is done once to select only forward look points and once to select only aft-look points. There is a special case where both aft and forward-look points might be mixed in the six points selection. This is the case when the closest point to the target point is close to a 90^o or 270^o scan angle.

$$\underbrace{0.3\ degrees}$$

(i+1,j-1)	*(i+1,j)*	*(i+1,j+1)*
(i,j-1)	*(i,j)*	*(i,j+1)*
(i-1,j-1)	*(i-1,j)*	*(i-1,j+1)*

Figure 6:Search scheme

3.2 Algorithm Flow

L1B_TB_E SPS reads the necessary information to perform BG interpolation from the input L1B_TB product. The input file is specified in the RunConfig file.

The BG optimal interpolation interpolates at a target point ($\bar{\rho}_d$) the antenna temperature at the top of the ionosphere after moon, galactic, and solar effect corrections were applied. We will refer to the antenna temperature on the top of the ionosphere after moon, galactic, and solar effect corrections were applied as ta_earth_v , $ta\_earth\_h, ta\_earth\_3, ta\_earth\_4$. The target points $\bar{\rho}_d$ are defined over a 9Km EASE2 grid.

The fields ta_earth_v , ta_earth_h, ta_earth_3 and ta_earth_4 are not provided as output in the L1B product but they can be reconstructed using two existing output values as follows:

$$ta\_earth\_p = toi\_p + antenna\_sidelobe\_correction\_p, \quad p = v, h, 3,4$$

"SMAP Algorithm Theoretical Basis Document: *L1B Radiometer Product"* details how those values are computed in the L1B_TB product in section 5.12.9.

The L1B_TB product defines toi_v as the vertically polarized apparent brightness temperature at the top of the ionosphere, toi_h as the horizontally polarized apparent brightness temperature at the top

of the ionosphere, toi_3 as the 3rd Stokes parameter at the top of the ionosphere, toi_4 as the 4th Stokes

parameter at the top of the ionosphere, $antenna\_sidelobe\_correction\_v$ as TB correction to TA for earth sidelobe contribution for vertical polarization, $antenna\_sidelobe\_correction\_h$ as TB correction to TA for earth sidelobe contribution for horizontal polarization, $antenna\_sidelobe\_correction\_3$ as TB correction to TA for earth sidelobe contribution for 3rd Stokes, and *antenna_sidelobe_correction_4* as TB correction to TA for earth sidelobe contribution for 4th Stokes.

We defined the interpolated antenna temperatures $\overline{ta\_earth\_p},\ p = v, h, 3, 4$ computed as:

$$\overline{ta\_earth\_p}\,(\bar{\rho}_d) = \sum_{i=0}^{N} a_i\ ta\_earth\_p(\bar{\rho}_i), \qquad p = v, h, 3, 4$$

where the $(\bar{\rho}_i),\ \text{with}\ i = 0 \ldots N$ are the selected SMAP measurements. We set $N = 6$ in our algorithm. The vector coefficient a is computed using equation (2.20). The selection of the SMAP measurements is detailed in 3.1.

Figure 7 summarizes the L1B_TB_E algorithm's flow.

3.2.1 Antenna Pattern Correction

After the interpolated values are obtained, we apply the Earth sidelobe correction, mainbeam efficiency and cross-coupling correction (antenna pattern correction)

$$\begin{bmatrix} \overline{toi\_v}(\bar{\rho}_d) \\ \overline{toi\_h}(\bar{\rho}_d) \\ \overline{toi\_3}(\bar{\rho}_d) \\ \overline{toi\_4}(\bar{\rho}_d) \end{bmatrix} = M \begin{bmatrix} \overline{ta\_earth\_v}(\bar{\rho}_d) \\ \overline{ta\_earth\_h}(\bar{\rho}_d) \\ \overline{ta\_earth\_3}(\bar{\rho}_d) \\ \overline{ta\_earth\_4}(\bar{\rho}_d) \end{bmatrix},$$

where $\overline{toi\_v}$, $\overline{toi\_h}$, $\overline{toi\_3}, \overline{toi\_4}$ are the apparent brightness temperatures and the 3rd and 4th Stokes parameters on the top of the ionosphere. The matrix M is the antenna pattern correction matrix. The antenna pattern correction matrix is an input file specified in the RunConfig file.

3.2.2 Faraday Rotation Correction

After the antenna temperature on the top of the ionosphere is obtained we apply the Faraday Rotation correction. We used the same algorithm to produce the L1B_TB product; see SMAP Algorithm Theoretical Basis Document: *L1B Radiometer Product*. The correction at the grid point $\bar{\rho}_d$ is computed using $\overline{toi\_v}$, $\overline{toi\_h}$, $\overline{toi\_3}$ and $\overline{toi\_4}$.

3.2.3 Atmospheric Correction

Atmospheric correction is applied to $\overline{toi\_v}$, $\overline{toi\_h}$, $\overline{toi\_3}, \overline{toi\_4}$.

The atmospheric correction consists of two steps:

1. Ancillary data interpolation
2. Atmospheric correction

Figure 7:Algorithm flow

Both steps use the same algorithm used to produce the L1B_TB product.

The ancillary data we use is specified in the RunConfig file. The ancillary files provide sea surface temperature (In RunConfig: "SeaSurfTemp") and pressure, water vapor, and air temperature (In RunConfig: "GEOS3HourInstantaneousData").

Before applying the atmospheric correction model, the ancillary data is interpolated over the 9 km EASE2 grid. The interpolated ancillary data can be found in the L1B_TB_E product as:

- *pressure aft*
- *pressure fore*
- *water_vapor_aft*
- *water_vapor_fore*
- *temperature_aft*
- *temperature fore*

The ancillary data is interpolated using bilinear interpolation in space and liner interpolation in time. The time interpolation requires each grid point to have an assigned time. The time we assign to each grid point is the weighted average time of the selected points we used to perform the interpolation,

$$\overline{time} = \frac{1}{N}\sum_{i=1}^{N} a_i time_i$$

where $\overline{time}$ is the interpolated time at the grid point $\bar{\rho}_d$ and $time_i$ is the time at the SMAP measurement at $\bar{\rho}_i$.

4 NEDT

All interpolation algorithms that use a weighted sum of neighboring data points inherently include a trade-off of resolution and noise. When the noise in the contributing data to the interpolation point value are equal and statistically independent, the final value of noise variance at the interpolation point is the sum-of-squares of the interpolation coefficients multiplied by the noise variance of each contributing data granule.

Since the sum of the weights in these interpolation methods is unity, the variance is always reduced when compared to any one contributing data granule. However, the distribution of the weights determines the degree to which the weighted averaging of noisy data results in reduced noise variance. The distribution of the weights (summing to unity) is also a factor in the beam sharpening (or broadening). Thus the distribution of the weights (summing to unity) controls the trade-off between noise variance reduction and resolution properties of interpolated field. The issue has subtle variations about this theme when the contributing data granules have overlapping field-of-view domains (see Section 1).

The variance of the interpolated antenna temperature is computed as:

$$e^2 = \sum_{i=1}^{N} a_i{}^2 NEDT_i{}^2$$

(Equation 12 in Stogryn, 1978; 6 in Migliaccio et al., 2005; 6 in Robinson et al., 1992). It results simply from the fact that in BG and many other interpolation techniques, the interpolated data is a linear combination of measurements. The random noise variance in the interpolated data is therefore the sum of squared weighting coefficients multiplied by the noise variance of the component measurements. The noise levels obtained are improved over L1B_TB single footprint measurements due to the interpolation performed, and are similar to the noise levels of the baseline L1C_TB product, which also performs an interpolation of single footprint measurements in mapping to a 36 km grid.

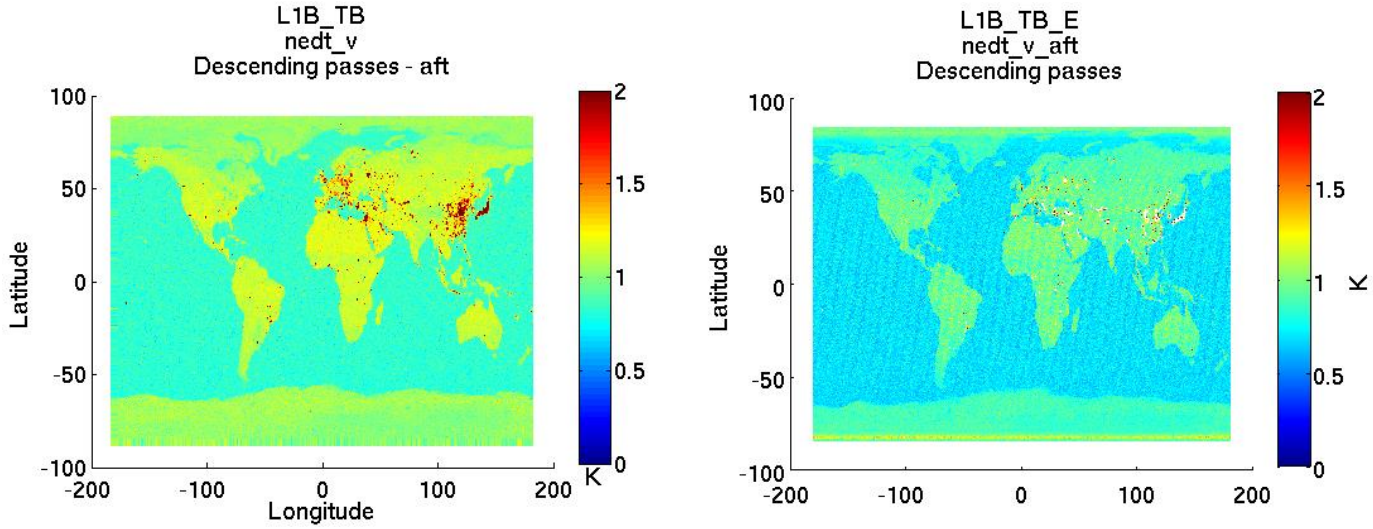

Figure 8:NEDT for V polarization corresponding to descending passes and aft looks. Left: L1B_TB. Right: L1B_TB_E.

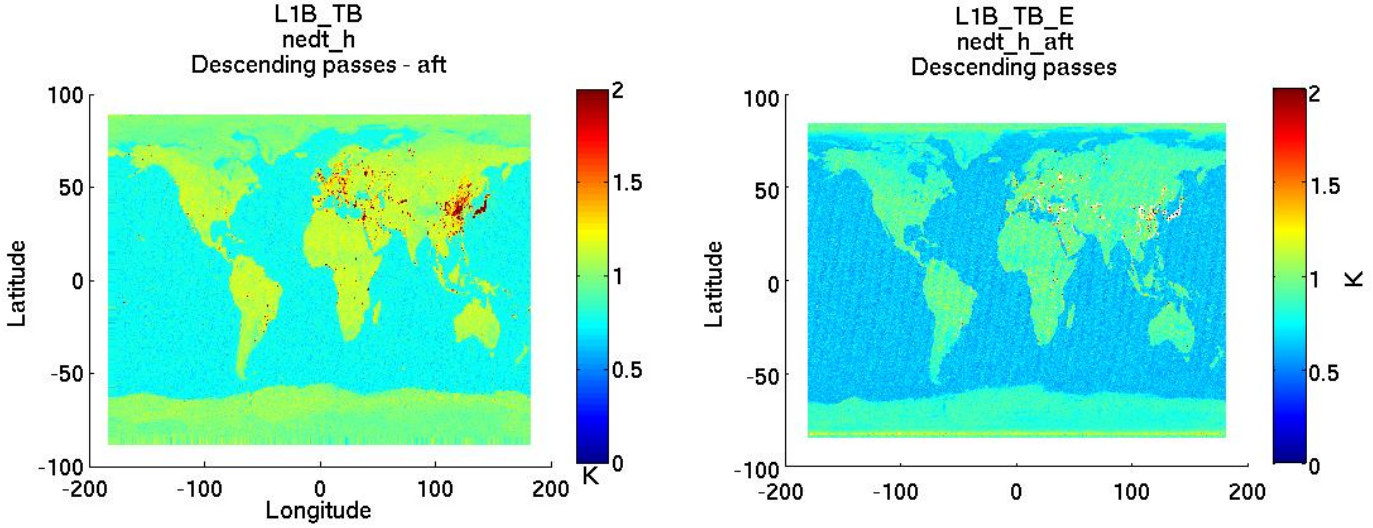

Figure 9: NEDT for H polarization corresponding to descending passes and aft looks. Left: L1B_TB. Right: L1B_TB_E.

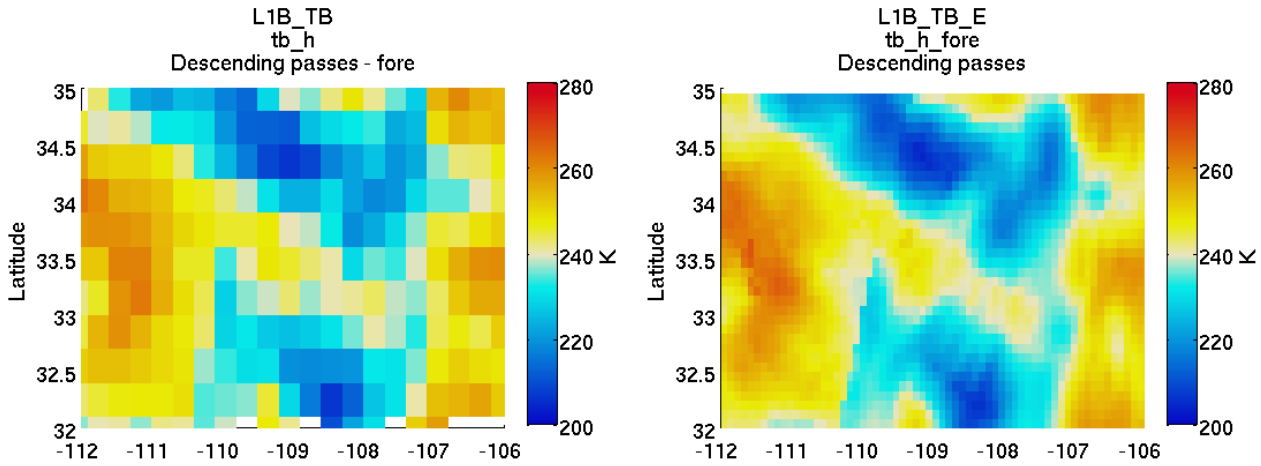

Figure 10: Image of Arizona during the three days period: 08/25, 08/26,08/27 20015. Left: L1B_TB product gridded over 0.3x0.3 degree cells. Right: BG optimal interpolated data gridded over 0.1x0.1 degree cells.

Figure 8 and Figure 9 show global maps of the *NEDT* corresponding to the interpolated antenna temperature for both polarizations, *V* and *H,* on the left those figures show the corresponding NEDT from the L1B_TB product. The examples correspond to descending passes and aft looks. Because the optimal interpolation field combines multiple measurements, its noise variance is lower than any one measurement as evident in Figure 8 and Figure 9.

5 Examples of Finer Details in Interpolated Images

The following examples, Figure 10, Figure 11Figure 12, show a close view of different areas. Overall, the examples show a significant improvement on the quality of the image. The figures on the

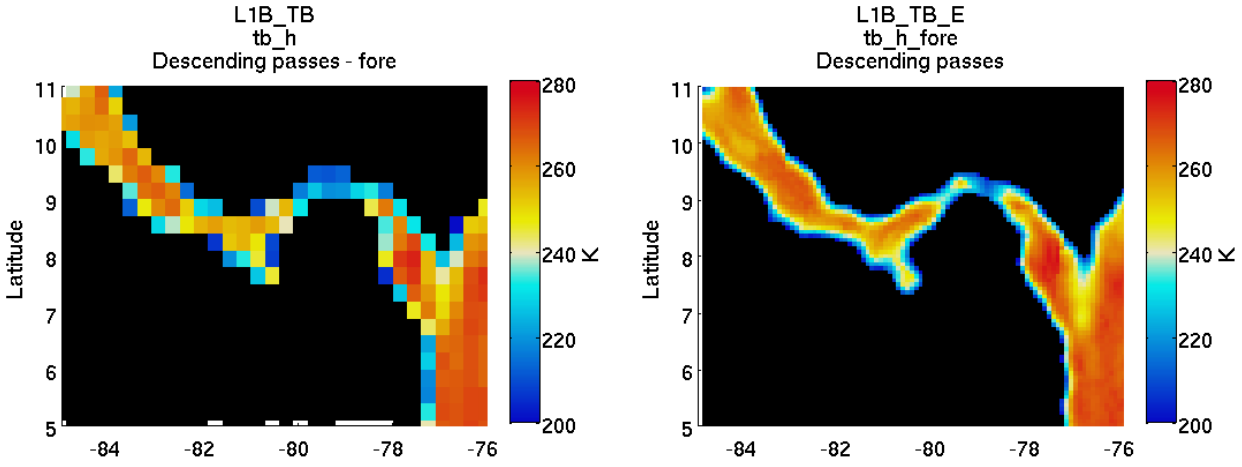

Figure 11: : Image of Panama during the three days period: 08/25, 08/26,08/27 20015. Left: L1B_TB product gridded over 0.3x0.3 degree cells. Right: BG optimal interpolated data gridded over 0.1x0.1 degree cells.

left display the L1B_TB product gridded over a 0.3x0.3 degree cells. This is the nominal SMAP gridding. The figures on the right display the L1B_TB_E product gridded over 0.1x0.1 degree cells.

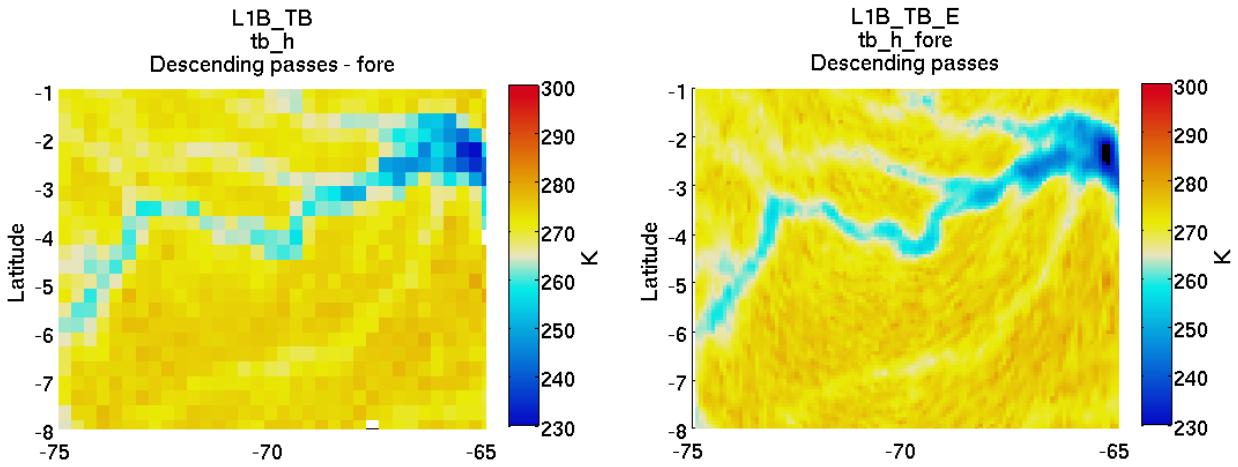

Figure 12: Image of Amazon during the three days period: 08/25, 08/26,08/27 20015. Left: L1B_TB product gridded over 0.3x0.3 degree cells. Right: BG optimal interpolated data gridded over 0.1x0.1 degree cells.

6 Water/Land Contamination Correction

In regions near the coast or near inland bodies of water, the SMAP footprint contains land and water, resulting in errors in the soil moisture estimation. The mixed land and water emissions lead to land brightness temperature underestimation and thus to the overestimation of soil moisture. Figure 13 displays a view of the Great Lakes. On the left, the figure shows the brightness temperature maps showing the smooth transition of the water/land interface due to land/water contamination (yellow and light blue colors). On the right, it shows the corresponding soil moisture map. The blue rings around the lakes are the result of water contamination.

The determination of the land and water temperatures contributing to the temperatures at the EASE2 grid points will not only have a significant impact on the reduction of the soil moisture errors near

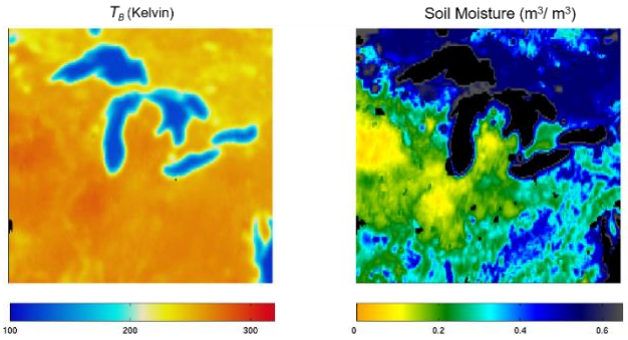

Figure 13: Left: Brightness temperature map of the Great Lakes showing yellow and light blue colors at the edges of the lakes caused by the land/water contamination. Right: Corresponding soil moisture map with presence of intense blue colors around the lakes due to overestimation of soil moisture.

coastal zones, but also on the retrieval of other physical parameters provided by the high level SMAP products.

In the L1B_TB_E product, the brightness temperatures are obtained after interpolating the contaminated antenna temperatures using the Backus-Gilbert algorithm described previously, thus the interpolated temperatures are also contaminated.

The L1B_TB_E algorithm, applies a single measurement technique to separate the land and water contribution for the uncorrected SMAP interpolated data over the EASE2 grid. In this document, we summarize the methodology for the retrieval of land and water brightness temperatures (Section 6.1). We then show results using simulated data (Section 6.2) and evaluate the performance of our approach. Finally, we show results using real data (Section 6.3). We assume that the sensitivity analysis detailed in Section 6.2 for the L1B_TB product is valid for the L1B_TB_E product, and therefore, the values of the threshold and the extent of the searching areas were applied to the L1B_TB_E product as well.

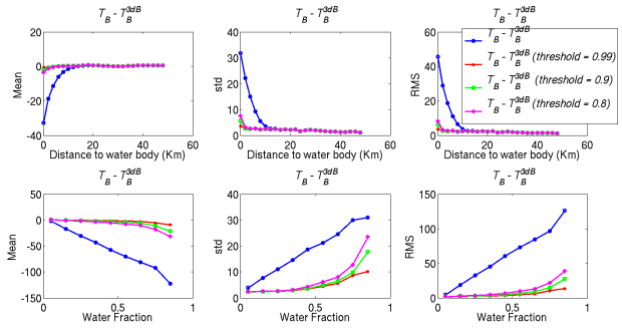

Figure 14: Mean, std, and RMSE resulting from the water contamination correction. We display the difference of uncorrected T_B - $T_{B_{land}}^{3dB}$ (blue line) and corrected T_B -$T_{B_{land}}^{3dB}$ for several thresholds (0.99, 0.9, 0.8). Top row displays statistics as a function of distance to water bodies. Bottom row displays statistics as a function of water fraction.

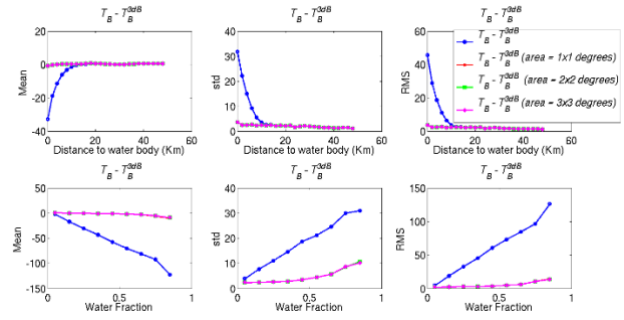

Figure 15: Mean, std, and RMSE resulting from the water contamination correction. We display the difference of uncorrected T_B - $T_{B_{land}}^{3dB}$ (blue line) and corrected T_B -$T_{B_{land}}^{3dB}$ for several searching areas (1x1

degrees, 2x2 degrees and 3x3 degrees). Top row displays statistics as a function of distance to water bodies. Bottom row displays statistics as a function of water fraction.

6.1 Retrieval Methodology for Water and Land Brightness Temperature

The brightness temperature T_B measured by the antenna can be modeled by the convolution of the antenna gain pattern with the actual distribution of brightness temperature T_b over the surface of the earth:

$$T_B(\hat{s}_0) = \frac{\int G(\hat{s}_0, \hat{s}) T_b(\hat{s}) d\Omega}{\int G(\hat{s}_0, \hat{s}) d\Omega}, \qquad (1)$$

where $\hat{s}_0$ is the center of the footprint projection, and $G(\hat{s}_0, \hat{s})$ is the antenna gain pattern center at $\hat{s}_0$ and evaluated over the surface point $\hat{s}$. Equation (1) can be separated into the land and water contribution as follows:

$$T_B(\hat{s}_0) = \frac{1}{\int G(\hat{s}_0, \hat{s}) d\Omega} \left(\begin{array}{l} \int G(\hat{s}_0, \hat{s}) \big(1 - M(\hat{s})\big) T_b(\hat{s}) d\Omega \\ \quad + \int G(\hat{s}_0, \hat{s}) M(\hat{s}) T_b(\hat{s}) d\Omega \end{array} \right),$$

where *M(x)* is a land mask defined over a 1Km EASE2 grid. *M(x)*=1 if *x* is over water and *M(x)*=0 if *x* is over land. Assuming that $T_b = T_B^{land}$ is constant over the land portion of the domain of integration and that $T_b = T_B^{water}$ is constant over the water portion of the domain of integration, then we have

$$T_B(\hat{s}_0) = (1 - f) T_B^{land} + f T_B^{water}, \qquad (2)$$

where *f* is the water fraction given by

$$f = \sum_{i=1}^{N} a_i f_i,$$

and a_i are the Backus-Gilbert coefficients used for the interpolation of the antenna temperature and f_i is the water fraction corresponding to the SMAP measurements used for the Backus-Gilbert interpolation and is given by

$$f_i = \frac{\int G(\hat{s}_0, \hat{s}) M(\hat{s}) d\Omega}{\int G(\hat{s}_0, \hat{s}) d\Omega},$$

To retrieve the land and water brightness temperature we separate our set of measurements into two sets according to the location of the grid point, one for grid points located over land and the other with grid points located over water. We first retrieve the brightness temperature over land and then we retrieve the brightness temperature over water as follows:

1. From equation (2) replacing T_B^{water} by an estimate $\hat{T}_B^{water}$, T_B^{land} can be obtained as:

$$T_B^{land} = \frac{T_B - f\hat{T}_B^{water}}{1-f},$$

To estimate the brightness temperature over water, $\hat{T}_B^{water}$, we search for measurements with the footprint center located over water and with a water fraction greater than a pre-fixed threshold (the sensitive study for the selection of the threshold is detailed in the next section) to assure the selection of contamination-free measurements. The extent of the searching region is also pre-fixed to assure that we can find measurements within it (the sensitive study for the selection of the extent of the searching area is detailed in the next section). If measurements satisfying the threshold condition are not found within the region then a default value is used. The default value is either the average of all the measurements on the half-orbit pass satisfying the threshold condition or the previously selected water brightness temperature.

2. From equation (2) replacing T_B^{land} by an estimate $\hat{T}_B^{land}$, T_B^{water} can be obtained as:

$$T_B^{water} = \frac{T_B - (1-f)\hat{T}_B^{land}}{f},$$

The estimation of the land temperature following a similar algorithm, as in item 1, is challenging due to the greater variance of the land temperatures. In addition, searching for measurements free of contamination requires looking into regions away from the coastal zones leading to averaged temperatures that might not be representative of the real coastal brightness temperature. Therefore, we apply an alternative method by modifying our algorithm to mitigate those challenges. Taking advantage of the already corrected land temperatures, as in item 1, we can reduce the searching area and allow for the selection of corrected temperatures closer to the coastal zone without imposing water fraction conditions (these measurements are no longer affected by contamination). Then we obtain the inverse distance weighted average temperature from temperatures already free of contamination.

Note that to avoid division for numbers close to zero we retrieve land brightness temperatures for measurements with water fraction smaller than 0.9 and we retrieve the water brightness temperatures with water fraction greater than 0.1. It is also important to note that we only apply correction if the sea ice fraction is equal to zero.

We also set some parameters to certify that the product was providing realistic temperature values when the water/land contamination correction failed to correct successfully:

1. Valid range for TB V polarization [50K: 340K]. Values outside this range are replaced with fill values.
2. Valid range for TB H polarization [30K: 340K]. Values outside this range are replaced with fill values.
3. Over land, if corrected TB < uncorrected TB then value is replaced with fill values.
4. Over water, if corrected TB > uncorrected TB then value is replaced with fill values

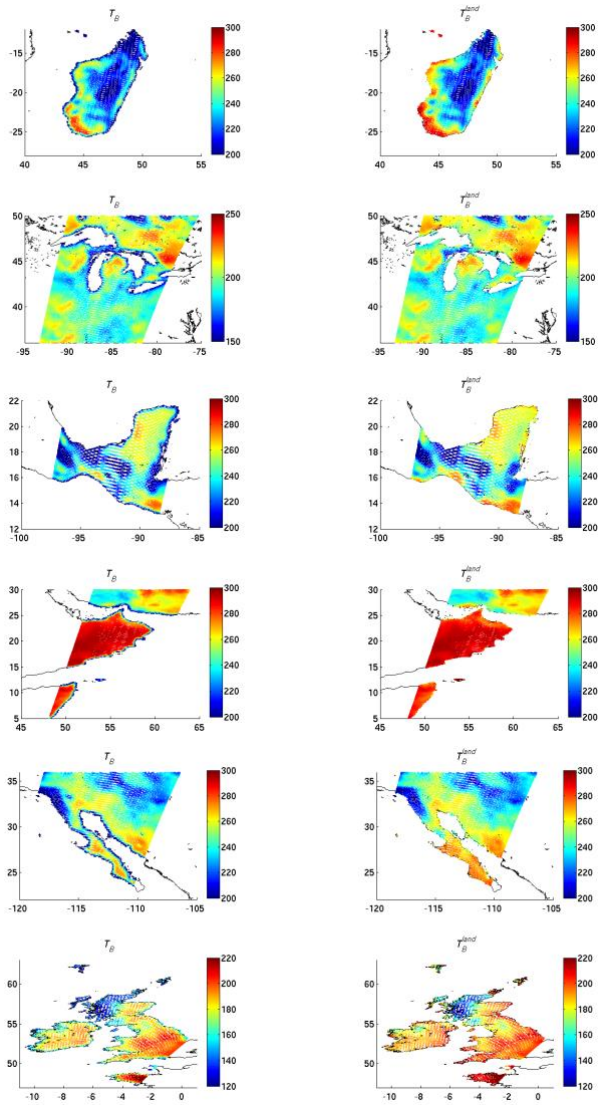

Figure 16: Results obtained using simulated data. Left: The SMAP simulated measurements before correction. Right: Corrected land brightness temperatures. From top to bottom we have: a) Madagascar, b) Great Lakes, c) Yucatan Peninsula, d) Arabian Sea, e) Baja California and f) United Kingdom.

6.2 Simulated SMAP Data and Retrieval Results

Our simulated SMAP measurement of the brightness temperature T_B follows equation (1), ignoring atmospheric and galactic effects. The emitted brightness temperature T_b over land surface is computed using a plane surface model taking into account the surface temperature, the frequency (1.414 GHz), the incidence angle (~40 degrees) and the dielectric constant which is computed using the Mironov's model (2008) Our land dielectric constant takes into account soil moisture content and clay fraction only (bare

soil). The model for the T_b over water follows the model presented by Yueh (2012). This model takes into account wind, sea surface temperature, and salinity.

To evaluate the performance of our algorithm to retrieve brightness temperature over land, we compare the uncorrected and corrected brightness temperature against the simulated brightness temperature contribution over the 3dB beam coming from land only

$$T_{B_{land}}^{3dB}(\hat{s}_0) = \frac{\int G(\hat{s}_0, \hat{s})(1 - M(\hat{s}))T_b(\hat{s})d\Omega_{3dB}}{\int G(\hat{s}_0, \hat{s})d\Omega_{3dB}},$$

where Ω_{3dB} is the 3dB beam domain of integration.

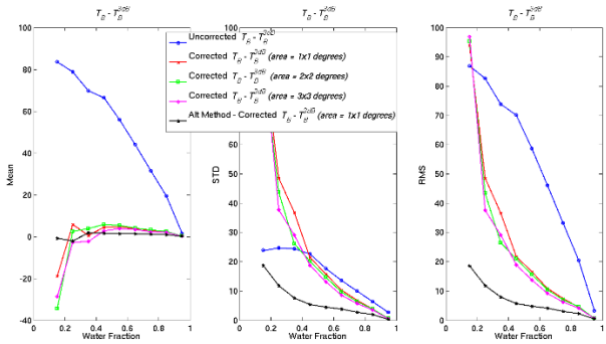

Figure 17: Statistics. Mean, std, and RMSE resulting from the land contamination correction as a function of water fraction. We display the difference of uncorrected T_B - $T_{B_{water}}^{3dB}$ (blue line) and corrected T_B -$T_{B_{water}}^{3dB}$ for several searching areas (1x1 degrees, 2x2 degrees and 3x3 degrees). We also incorporate the results obtained using the alternative method (black line).

The T_B and $T_{B_{land}}^{3dB}$ were simulated for six different earth regions and then the corrected T_B^{land} was computed as it was stated in the previous section in item 1. The uncorrected T_B and the corrected T_B^{land} were compared against $T_{B_{land}}^{3dB}$. Before applying our algorithm, two parameters (water fraction threshold and the dimensions of the searching area) need to be set in order to estimate $\hat{T}_B^{water}$. Figure 14 displays the mean, standard deviation (std) and the root mean square (RMS) of the differences, ($T_B - T_{B_{land}}^{3dB}$), as a function of distance to water bodies (top row) and as a function of water fraction (bottom row) for different thresholds values. To evaluate the statistics as a function of distance to water bodies, we binned the data into 2km bins and then the mean, std and RMS of differences were evaluated for each bin. To evaluate the statistics as a function of water fraction the data were binned into 0.1 water fraction increments. Those results show that the performance improves when the threshold gets closer to one (red line). We also observe that the performance deteriorates as the water fraction tends to one (footprint on small pieces of land surrounded by water). Figure 15 displays the statistics from results obtained for different searching area dimensions showing that the size of the area does not affect the incoming results. Thus, based on our sensitivity results we set the water fraction threshold to 0.99 and the searching area dimension to 3x3 degrees in a latitude and longitude to assure we have enough measurements within the area under consideration satisfying the threshold condition. Figure 16 displays maps of the uncorrected land T_B (left) and the corrected T_B^{land} for several regions. We can notice that the smooth transition between land and water was eliminated after correction creating sharper edges.

We then retrieve T_B^{water} as stated in item 2 of the previous section and we compare it against the corresponding 3 dB brightness temperature contribution from water given by

$$T_{B_{water}}^{3dB}(\hat{s}_0) = \frac{\int G(\hat{s}_0, \hat{s}) M(\hat{s}) T_b(\hat{s}) d\Omega_{3dB}}{\int G(\hat{s}_0, \hat{s}) d\Omega_{3dB}}.$$

To estimate $\hat{T}_B^{land}$ we need to set the dimension of the searching area. Figure 17 displays the statistic results for corrected water brightness temperatures comparing results for different cases: area dimension 1x1 degrees, 2x2 degrees, and 3x3 degrees and water fraction threshold set to 0.99. We also add results for the suggested alternative method as explained in item 2 setting the searching area to 1x1 and allowing the selection of already corrected temperatures. The figure shows that the performances are very similar for the first three cases and the solution improves significantly when the alternative method is used (black line).

In view of those results, the searching area for the estimation of $\hat{T}_B^{land}$ was set to 1x1 degree and the alternative method was applied. From Figure 17 looking at the alternative method results (black line), we see that the mean values stay between -2 to 2 Kelvins (K) and the std and RMS are ~19K for lower water fractions (footprint on small bodies of water) and decrease rapidly reaching ~5K when the water fraction is ~0.5. Maps of uncorrected water T_B and corrected T_B^{water} are displayed in Figure 18. We can see how the dark edges on the left column maps disappear after correction.

6.3 Real SMAP Data Results

The results over real data were obtained following the same algorithm described in the previous section. We should not expect the same performance obtained with simulated data due to the presence of other sources of errors when dealing with real data such as geolocation errors, greater variability of brightness temperature (vegetation, urban areas…), etc. Maps showing results using real data are displayed in Figure 19 and Figure 20. In Figure 19 we can observe that the intense blue borders corresponding to cold temperatures in the coastal areas were removed after correction. Figure 20 shows the uncorrected and corrected brightness temperature over ocean. We can see in some areas that the corrected brightness temperatures over ocean are underestimated. We suspect that residual pointing errors maybe the cause of those anomalies. Figure 9 and 10 display scatter plots of T_B as a function of water fraction before and after correction for the different regions. It can be observed that after correction all dependence on water fraction was eliminated. Detailed information about the data used in this section can be found in the Internal documents Chaubell (2016), Chan (2016) and Piepmeier (2016).

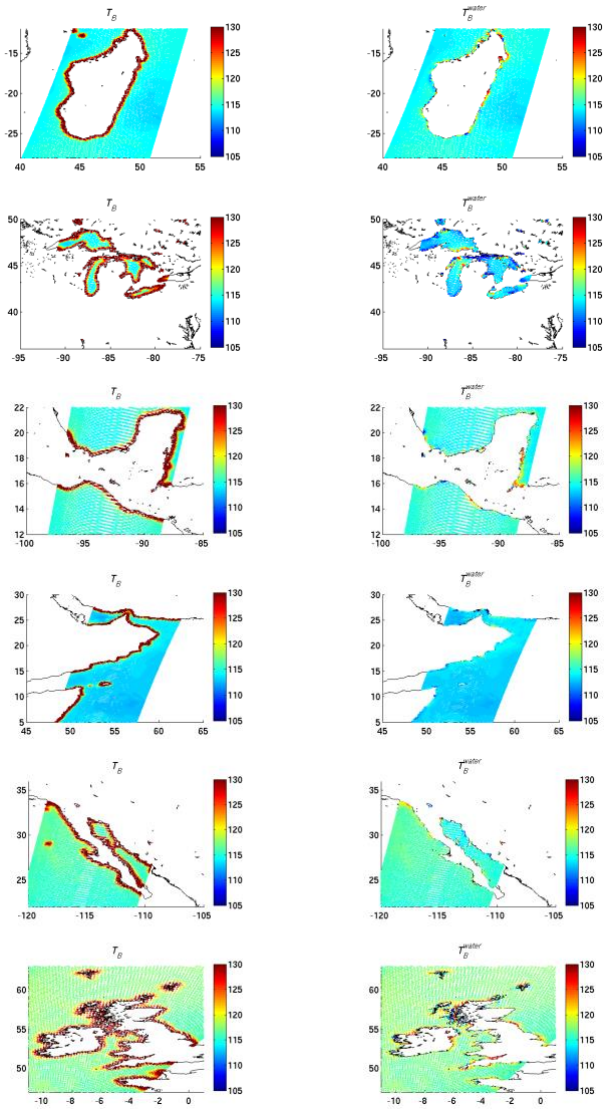

Figure 18: Results obtained using simulated data. Left: The SMAP simulated measurements before correction. Right: Corrected water brightness temperatures. From top to bottom, we have a) Madagascar, b) Great Lakes, c) Yucatan Peninsula, d) Arabian Sea, e) Baja California and f) United Kingdom.

6.4 Conclusion

An algorithm to improve the brightness temperature measurements over coastal areas and near bodies of water was implemented. Overall, our algorithm performed very well. Results over simulated data show significant statistical improvements. Results over real data show that our algorithm eliminates the cold borders over land and the warmer borders over ocean. The dependence on water fraction was eliminated after correction. Some anomalies, however, need still being investigated and resolved.

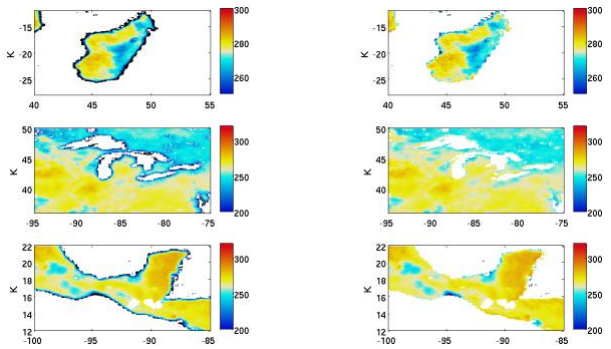

Figure 19: Results over land using SMAP measurements. Left: uncorrected data. Right: corrected land brightness temperature.

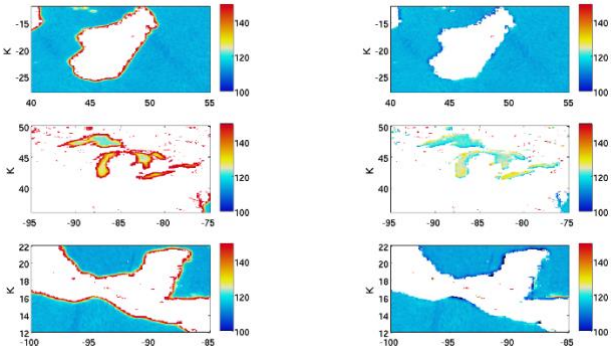

Figure 20: Results over land using SMAP measurements. Left: uncorrected data. Right: corrected water brightness temperature.

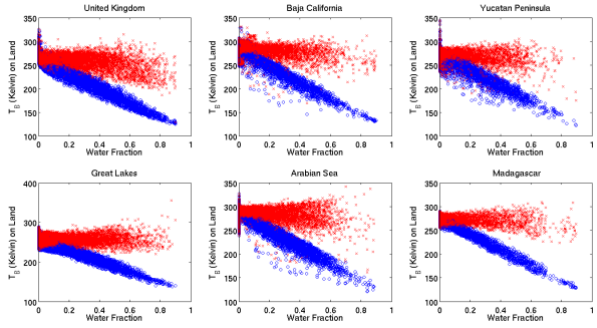

Figure 21: Scattering plot of uncorrected T_B (blue circles) and corrected land T_B (red times) as a function of Water fraction. From left to right; Top: United Kingdom, Baja California and Yucatan Peninsula; Right: Great Lakes, Arabian Sea and Madagascar. Before correction the T_B decrease with land fraction and after correction, we remove that dependence.

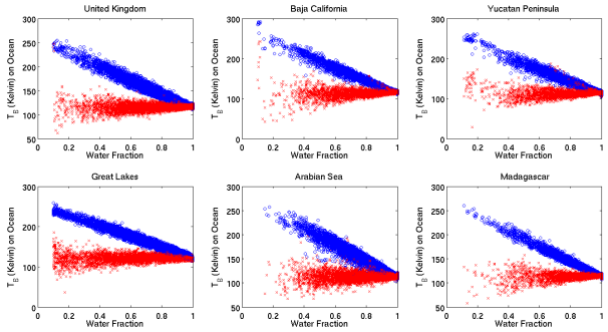

Figure 22: Scattering plot of uncorrected T_B (blue circles) and corrected water T_B (red times) as a function of Water fraction. From left to right; Top: United Kingdom, Baja California and Yucatan Peninsula; Right: Great Lakes, Arabian Sea and Madagascar. Before correction the T_B decrease with land fraction and after correction, we remove that dependence.

7 Notes About the Product

The L1B_TB_E product contains four data groups:

- Metadata
- Brightness temperature
- North polar projection
- South polar projection

The EASE2 Grid consists of a set of three equal-area projections: the global cylindrical equal-area (CEA), and the Northern and Southern hemisphere azimuthal equal area (AEA) projections (see Figure 23). The L1B_TB_E data product includes output files in each of these three projections. The Brightness Temperature group provides all the fields over a global EASE2 grid.

All the fields in the product that come from fields in the L1B_TB product are obtained by interpolation. The BG coefficients are used to interpolate those fields at the target point $\bar{\rho}_d$. If the location of the target point $\bar{\rho}_d$ coincides with the location of some of the $\bar{\rho}_i$ SMAP measurements, m_i, $i = 1 \ldots N$, the BG coefficients will be all zeros except for a_i, the one multiplying m_i and thus, the assigned value at the target point $\bar{\rho}_d$ will be the same value that corresponds to $\bar{\rho}_i$.

The flag bits are the same as the flags' bits in the L1B_TB product. The flags are set to "1" if one or more of the six selected points used to perform the interpolation has the flag set to "1".

The L1B_TB_E product contains some additional outputs fields that are related to the BG algorithm. They are:

- bg_coefficients_aft and bg_coefficients_fore:

These are three dimensional arrays containing the BG coefficients *a* used to performed the interpolation.

- bg_scan_aft and bg_scan_fore:
  These are three dimensional arrays containing the L1B_TB scan corresponding to the SMAP measurements used in the interpolation.

- bg_rev_aft and bg_rev_fore:
  These are three dimensional arrays containing the L1B_TB rev corresponding to the SMAP measurements used in the interpolation. Note that these two arrays combining with bg_scan_aft and bg_scan_fore give the exact location on the L1B_TB product of the SMAP measurement used for the interpolation.

- regularization_factor_aft and regularization_factor_fore:
  These are two dimensional arrays containing the regularization parameter ε that is used to obtain the interpolated value at the grid point, see Figure 3. Regularization is only applied when the noise amplification factor $\sum_{i=1}^{N} a_i^2 > 1$, where N = 6 in our implementation.

The North and South Polar Projection Groups contains all the same fields as the Brightness Temperature

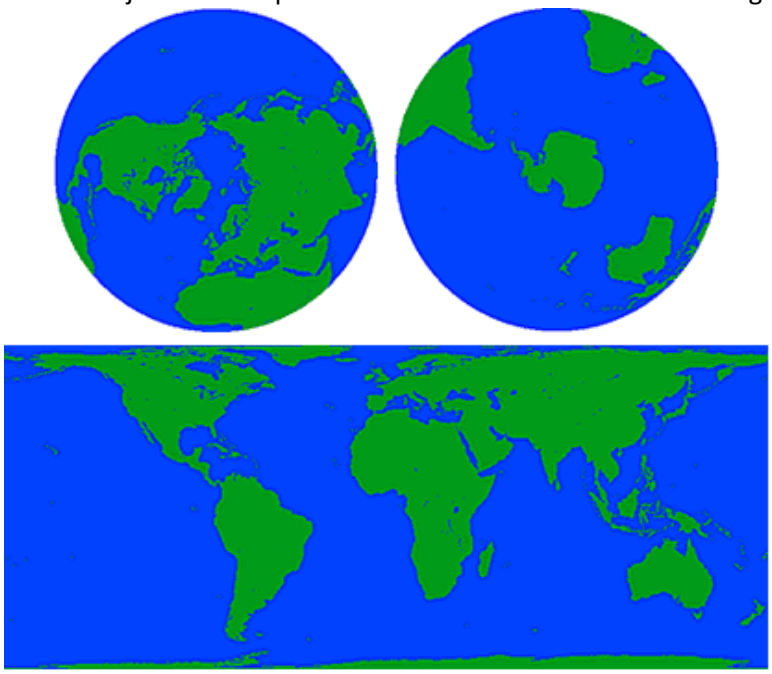

Figure 23: The EASE-Grid Projections. Northern Hemisphere (top left), Southern Hemisphere (top right) and global (bottom). Although these figures describe the original EASE-Grid formulation, they are also valid for the visualization of the newer EASE-Grid 2

group but in these cases the values are over the North and South Polar projection grids respectively, Figure 23.

A complete description of the contents of the L1B_TB_E data product is contained in the SMAP L1B_TB_E Data Product Specification document.

8 Acknowledgment

The research was carried out at the Jet Propulsion Laboratory, California Institute of Technology, under a contract with the National Aeronautics and Space Administration.

9 References

G. Backus and F. Gilbert, "Uniqueness in the inversion of inaccurate gross earth data," Phil. Trans. R. Soc. London, vol. A266, Mar 1970.

P. Chakraborty, Misra A, Misra T. and Rana S.S. "Brightness Temperature Reconstruction Using BGI". IEEE Trans. Geosci. Remote Sensing, vol.46, pp. 1768-1773, May.2008.

D. Entekhabi et al. "The Soil Moisture Active Passive (SMAP) Mission," Proceedings of the IEEE, vol. 98, no. 5, pp. 704-716, May 2010.

M. R. Farrar and E. A. Smith, "Spatial resolution enhancement of terrestrial features using deconvolved SSM/I brightness temperatures," IEEE Trans. Geosci. Remote Sensing, vol.30, pp.349-355, Mar. 1992.

D. Long, "Reconstruction and resolution enhancement techniques for microwave sensors", in Frontiers of Remote Sensing Information Processing", C. H. Chen (editor), 255-281, 2003;

D. Long, and D. Daum, "Spatial resolution enhancement of SSM/I data", IEEE Tans. Geosci. Remote Sensing, 36(2), 407-417, 1998.

Migliaccio M. and A. Gambardella, "Microwave Radiometer spatial resolution enhancement", IEEE Trans. Geosci. Remote Sensing, 43(5), 1159-1169, 2005.

G. Poe, "Optimum Interpolation of Imaging Microwave Radiometer Data", IEEE Transactions on geoscience and remote sensing, vol. 28. NO. 5, pp. 800-810. Sept. 1990.

W.D Robinson, C. Kummerow, and W. S. Olson, "A technique for enhancing and matching the resolution of microwave measurements from SSM/I instrument," IEEE Trans. Geosci. Remote Sensing, vol. 30, pp. 419-429, May 1992.

R. Sethmann, B. A. Burns, and G. C. Heygster, "Spatial resolution improvement of SSM/I data with image restoration techniques," IEEE Trans. Geosci. Remote Sensing, vol.32, pp. 1144-1151, Nov. 1994.

A. Stogryn, "Estimates of brightness temperatures from scanning radiometer data", IEEE Trans.Antennas propagat., vol.Ap-26, pp.720-726, Sept. 1978.

D.G. Long and M.J. Brodzik, “Optimum Image Formation for Spaceborne Microwave Radiometer Products,” IEEE Transactions on Geoscience and Remote Sensing, Vol. 54, No. 5, pp. 2763-2779, doi:10.1109/TGRS.2015.2505677, 2016.

Mironov, V. L., L. G. Kosolapova, and S. V. Fomin, \Soil dielectric model accounting for contribution of bound water spectra through clay content," *PIERS Online*, Vol. 4, No. 1, 31{35, 2008.

S. Yueh and J. Chaubell, “Sea surface salinity and wind retrieval using combined passive and active L-band microwave observations,” *IEEE Trans. Geosci. Remote Sens.*, vol. 50, no. 4, pp. 1022–1032, Apr. 2012.

J. Chaubell et al., "Improving Brightness Temperature Measurements Near Coastal Areas for SMAP," in IEEE Journal of Selected Topics in Applied Earth Observations and Remote Sensing, vol. 12, no. 11, pp. 4578-4588, Nov. 2019, doi: 10.1109/JSTARS.2019.2951323.

Internal Reference Documents

SMAP Algorithm Theoretical Basis Document: *L1B Radiometer Product*. SMAP Project, GSFC SMAP-006,

NASA Goddard Space Flight Center, Greenbelt, MD.

Theoretical Basis Document: Level 1C Radiometer Data Product , S. Chan, E. Njoku and A. Colliander. JPL D-53053, 2014.

D-56289_SMAP_Radiometer_Level_1B_TB_E_Product_Specification_Document, J. Chaubell, R. Dunbar, Jet Propulsion Laboratory, California Institute of Technology, Pasadena, CA, 2016.

Chaubell, M. J., S. Chan, R. S. Dunbar, J. Peng, and S. Yueh. 2016. *SMAP Enhanced L1C Radiometer Half-Orbit 9 km EASE-Grid Brightness Temperatures, Version 1*. Boulder, Colorado USA. NASA National Snow and Ice Data Center Distributed Active Archive Center. doi: http://dx.doi.org/10.5067/2C9O9KT6JAWS.

Chan, S., Njoku, E., Colliander, A. 2016. *SMAP L1C Radiometer Half-Orbit 36 km EASE-Grid Brightness Temperatures*. Version 3. Boulder, Colorado USA: NASA National Snow and Ice Data Center Distributed Active Archive Center. doi:http://dx.doi.org/10.5067/E51BSP6V3KP7.

Piepmeier, J. R., P. N. Mohammed, J. Peng, E. Kim, G. De Amici, and C. Ruf. 2016. *SMAP L1B Radiometer Half-Orbit Time-Ordered Brightness Temperatures*. Version 3. Boulder, Colorado USA: NASA National Snow and Ice Data Center Distributed Active Archive Center. doi:http://dx.doi.org/10.5067/YV5VOWY5V446.